

Deformation mechanism of strain localization in 2D numerical interface tests

Huaxiang Zhu¹ · Wan-Huan Zhou^{1,2}  · Zhen-Yu Yin³

Received: 9 November 2016 / Accepted: 2 May 2017 / Published online: 19 May 2017
© Springer-Verlag Berlin Heidelberg 2017

Abstract Heterogeneity arises in soil subjected to interface shearing, with the strain gradually localizing into a band area. How the strain localization accumulates and develops to form the structure is crucial in explaining some significant constitutive behaviors of the soil–structural interface during shearing, for example, stress hardening, softening, and shear-dilatancy. Using DEM simulation, interface shear tests with a periodic boundary condition are performed to investigate the strain localization process in densely and loosely packed granular soils. Based on the velocity field given by grains’ translational and rotational velocities, several kinematic quantities are analyzed during the loading history to demonstrate the evolution of strain localization. Results suggest that tiny concentrations in the shear deformation have already been observed in the very early stage of the shear test. The degree of the strain localization, quantified by a proposed new indicator, α , steadily ascends during the stress-hardening regime, dramatically jumps prior to the stress peak, and stabilizes at the stress steady state. Loose specimen does not develop a steady pattern at the large strain, as the deformation pattern transforms between localized and diffused failure modes. During the stress steady state of both specimens, remarkable correlations are observed between α and the shear stress, as well as between α and the volumetric strain rate.

Keywords DEM · Interface shearing · Soil–structure interface · Strain localization

1 Introduction

The soil–structural interface (SSI) exists in a variety of engineering situations, including pile engineering, soil nailing, and the application of geotextiles. It plays a fundamental role in engineering systems’ local and global stability and safety. The engineering community has long-term interest in SSI’s mechanical behaviors. A rich set of SSI’s constitutive features has been explored, such as the stress–displacement associated with the material’s parameters and surface geometry [9, 12, 26, 35, 40–42], the developing strain localization and the formation of structure [21, 42, 53], and the shear-induced fabric anisotropy of the soil [50, 51].

As a typical boundary value problem, heterogeneity arises in soil subjected to interface shearing and somehow develops along loading history. In this case, the strain will gradually localize into a band-shaped shear zone covering the rough surface, while the soil outside this zone, as a whole, undergoes quasi-elastic unloading. Out of the escalating degree of strain localization, a band with highly localized strain (called hereafter as localized band) will finally form at the large strain and show its characteristic highly concentrated soil deformation. Once this localized band stabilizes, the soil appears to be structurized into two domains with distinct deformational patterns: (1) the inside localized band area, featured by a large and non-affine deformation and (2) the remainder, with affine or even vanished shear deformation (the term “affine” refers to a constant displacement or velocity gradient). Meanwhile, macro- and micro-mechanical properties also structurize in

✉ Wan-Huan Zhou
hannahzhou@umac.mo

¹ Department of Civil and Environmental Engineering, Faculty of Science and Technology, University of Macau, Macau, China

² UMacau Research Institute, Zhuhai, Guangdong, China

³ Institut de Recherche en Génie Civil et Mécanique, Ecole Centrale de Nantes, LUNAM University, Nantes, France

association with this deformational heterogeneity [11, 14, 57]. Following these facts, on the one hand, SSI is essentially the interaction between the structure surface and the soil layer nearby [55]. SSI's nonelastic nature and shear resistance derive from this mechanical system. On the other hand, the strain localization process therefore plays a significant role in SSI's mechanical performance. Clarifying how strain localization accumulates and develops to form the localized band is crucial in explaining some of SSI's significant constitutive behaviors during the shearing, for example, stress hardening, softening, and shear-dilatancy.

In fact, the strain localization in SSI belongs to a general phenomenon, the localized failure in granular soils, which is considered as a bifurcation for the material from the homogeneous deformation pattern to a discontinuous one. During this geometrical transformation of the material, even for experiments conducted in identical conditions, various possible patterns can be encountered, leading to various post-bifurcation mechanical responses. It has been decades since scientists paid attention to strain localization and localized failure in the granular soil. Many studies have investigated the behavior and morphology of this type of failure from experimental [10, 11, 13, 44, 45] and theoretical viewpoints [4, 5, 15, 29, 34, 36–38, 45]. Of note, much research has focused on exploring the micro-mechanical basis of localized failure and the strain localization process. Characteristic microscale properties, such as particle rotation, fabric anisotropy, and force-chains, were observed to develop in association with the localized strain [2, 14, 16, 39, 48, 57, 58]. Notably, recent advances in multiscale modeling of strain localization in account for fabric anisotropy were reported [17–20, 56], which provide direct ways and new insights into correlative macroscopic observations of failure patterns in a boundary value problem. The influence of some micro-mechanical parameters on the formation of the localized band was revealed (see, for instance [23, 30, 43]). Exploring the strain localization process in SSI, as a typical and simple pattern of localized failure, from macro- and micro-viewpoints will contribute to the knowledge about the mechanism of the localized failure in soil.

Under the continuum-mechanical framework, determining the thickness of the localized band becomes important in the modeling of SSI. It is often required to define the interface zone, inside which the material will be treated with a different constitutive relation from the material outside the localized band. By adopting different criteria to detect the localized band boundary, some researchers have drawn varying conclusions [8, 53, 54]. In particular, Wang et al. [52], using DEM simulation, investigated the development of strain localization in densely packed granular soil sheared by interfaces of various roughness. Several characteristic points in the strain

localization process were pointed out. The influence of surface roughness on localized band thickness was reported in the authors' study. Even though the localized band thickness has been determined in various loading conditions and interface geometries, without understanding how the localized band emerges from the small-scale strain localization and develops to its final form in SSI, the relation between localized band thickness and its factors (the surface roughness, initial void ratio, confining stress, etc.) can be only empirical and lacks a physical background. However, scant work has engaged in this point.

This paper investigates the strain localization process in densely and loosely packed granular soils subjected to interface shearing. The following two aspects are focused: (1) How the pattern arises from a homogeneous deformation, evolves, and gives birth to a band with high strain localization and (2) how this evolution relates to the mechanical responses of SSI during shearing. Interface shear tests using DEM are introduced in Sect. 2 with modeling parameters, the test protocol, and some preliminary results. Methods of analyzing the kinematic field in the soil are given in Sect. 3. A mesoscale strain rate tensor is presented to define the local average strain inside individual polygonal cells enclosed by neighboring contact branches. This local strain rate tensor allows the strain field to form in the granular soil in a way where strain localization becomes conspicuous and can be conveniently captured and measured. We conduct comprehensive analyses on the kinematics of specimens in Sect. 4. A new indicator is proposed to characterize the degree of the strain localization. The evolutions of the shear velocity field, the shear velocity gradient, and the particle rotation are presented. In Sect. 5, evolutionary patterns and features of strain localization and their dependency on shear stress and volumetric strain are discussed for dense and loose specimens.

2 2D interface shear test

2.1 Numerical modeling and test protocol

The discrete element method (DEM) proposed by Cundall and Strack [7], coded by PFC2D 5.0 software in this study, is employed to solve the dynamics of the granular assembly subjected to interface shear loading. The interaction between two contacting objectives (particle–particle or particle–wall) is defined by the friction-elastic law, the combination of Hooke's law with a constant normal and tangential stiffness k_n and k_s , and the cohesionless Coulomb's law. To mimic the interlocking effect caused by the irregular shape of soil grains in natural soil, a rolling resistance is imposed onto contacts [23].

As illustrated in Fig. 1, the test apparatus, in width $w = 0.1$ m along the x -axis and in height $h = 0.04$ m along the y -axis, is constituted of a top wall and a teeth-plate on the bottom, as the latter assimilates the surface of the artificial structure, whose maximum y coordinate is set at $y = 0.0$ m. The teeth-plate is regularly shaped by segments of slope alternating between 45° and 135° . Its roughness R is quantified by λ/D_{50} , where λ is the vertical span of the teeth-plate. To avoid the boundary effect along the shear direction, a periodic boundary condition is set on both sides of the apparatus. In other words, particles passing through one side will appear on the counter-side with the same velocity. It is important to note that we chose a regular surface geometry for this study instead of an irregular one based on the following two considerations: (1) The main interest of this paper is the evolutionary feature of strain localization in the soil, rather than the effect of surface geometry on SSI's mechanical behavior, and (2) the surface geometry of an artificial structure is distinct in various situations; depending on the nature of the material and the way the structure is fabricated, no single pattern can be representative for all kinds of structures. Research on the mechanical behavior of SSI with various surface geometries includes works by Dove and Jarrett, Wang et al., and Wang and Jiang [12, 47, 49, 52]. Otherwise, we chose the specimen's height h in reference to the study given by Wang and Gutierrez [46], in which a minimum $40D_{\max}$ is suggested for h to sufficiently minimize the boundary effect of the apparatus to the direct shear test. As the direct shear test is normally constituted of two shear frames vertically symmetrical with each other, each frame can be basically equivalent to an interface shear box sheared by the soil contained in another frame. To this extent, a minimum $20D_{\max}$ is optical for h in the interface shear test. A much higher value $h = 0.04$ m (around $51D_{\max}$) is chosen in this study.

The specimen is installed by filling 12,000 particles into the test apparatus. To obtain a specimen with a relative isotropic initial fabric, the installation scheme for granular specimens proposed by Chareyre and Villard [6] is adopted by simultaneously growing the size of all particles, which are initially seeded over the apparatus's space with the

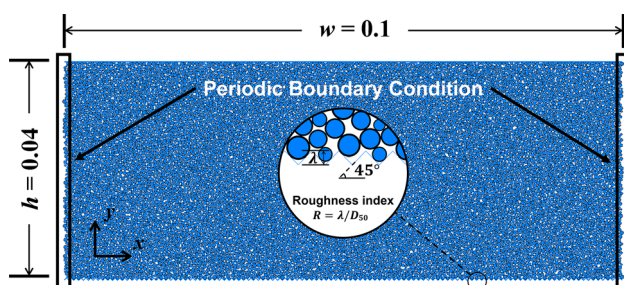


Fig. 1 Schematic diagram of the interface shear apparatus

diameter following a uniform distribution. This process stops once the normal stress on the top wall σ_n reaches the prescribed value. All grains in the specimen, whose radii are fixed afterward, form a poly-dispersed granular system with the grains' diameters uniformly varying in the range [0.374, 0.781 mm] and an average diameter of $D_{50} = 0.578$ mm. Then, φ_g is progressively vanished while maintaining σ_n to obtain a series of specimens with reduced initial void ratio of e_0 , wherein $e = V_{\text{void}}/V_{\text{solid}}$, as V_{void} and V_{solid} are, respectively, the total volume of the void and solid parts in the domain of measurement. After specimens are initialized with a certain value of e_0 , a constant shear velocity v_s is applied on the teeth-plate. It is noteworthy that v_s herein is sufficiently small to maintain the quasi-static state of the granular system; namely, the total inertia of this system is negligible, as this paper only aims to investigate the system's time-independent properties. The parameters used in numerical modeling are listed in Table 1.

2.2 Interface shear tests

The densest and loosest specimens among a series of prepared specimens, listed in Table 2, are chosen to carry out the interface shear test. In each monitoring strain state, the shear stress σ_s , the shear displacement d_s of the teeth-plate, and the volumetric strain ε_v of the specimen are measured as $\varepsilon_v = (h_t - h_0)/h_0$, where h_0 and h_t are heights of the specimen h (the distance between the top wall and the peak of the teeth-plate), respectively, at the initial state and the monitoring state. Evolutions of stress ratio σ_s/σ_n and ε_v with respect to normalized shear displacement d_s/D_{50} are shown in Fig. 2.

Two specimens converge into a single final value of σ_s/σ_n . S1 presents a stress peak and stress softening, while S2 does not see large-scale stress softening. In terms of volumetric evolution, S1 dilates from the beginning,

Table 1 Parameters in the simulation

Parameters	Value
k_n	5.0×10^9 N/m
k_t/k_n	0.5
Number of particles	12,000
Particle density	2650.0 kg/m ³
φ_g	26.57°
Particle–wall friction	41.99°
σ_n	1.0×10^5 N/m ²
v_s	2.0×10^{-3} m/min
R	0.75
Rolling resistance coefficient	0.1
Damping coefficient	0.1

reaches the highest dilatant rate at around the stress peak, and turns to a steady dilatancy when the stress residual state is reached. S2 experiences a slight contractancy at the beginning of the test and smoothly dilates afterward. Generally, the denser specimen tends to have a higher stress peak and a larger degree of dilatancy.

3 Velocity field and its gradient

Investigating the formation process of the localized band should be based on the kinematic analysis of the granular system. The means of analyzing the velocity field and building the strain rate field will be introduced in this section.

3.1 Analyzing the velocity field

The kinematic aspect of the granular system can be largely represented by the discrete field consisting of the translational velocity on the particle centers \vec{v}^p . Considering the horizontal velocity v_x^p , the velocity along the shear direction, the moving average is processed to smooth the fluctuation on the velocity field. As shown in Fig. 3, a thin rectangular window is set for measuring the average velocity \vec{v}_x of all contained particles inside it and is then moved along the y-axis to test the value of \vec{v}_x as a function of y, namely $\vec{v}_x(y)$.

3.2 Strain rate field

At any quasi-static state of a granular assembly, most grains are well supported by contacts with their

neighbors. Contact branches, connecting the centers of two contacting grains, distribute throughout the material, forming a network, named the contact network. By the contact network, the material area can be seamlessly tessellated into polygonal loops, denoted as meso-loops, enclosed by contact branches (as shown in Fig. 4). The equivalent continuum is assumed inside meso-loops in this study. The translational velocity field on a meso-loop is defined in such a way that the velocity at each vertex is equivalent to the velocity of associated grain with it, and the velocity along the contact branch keeps linear. Based on this velocity field, Kuhn [27, 28] derived a formula to define the average strain rate field of meso-loops. We exemplify this definition with a pentagon, highlighted in red in Fig. 4 and illustrated with local geometrical and kinematic quantities in Fig. 5. Vertices and edges are, respectively, numbered in a clockwise order. For the meso-loop i ($i = 1, 2, \dots, N_l$), where N_l is the total number of meso-loops, \hat{v}^{ij} denotes the relative velocity vector on the edge j , which is equal to $\mathbf{v}^{ij+1} - \mathbf{v}^{ij}$ (\mathbf{v}^{ij} is the velocity vector at vertex j), and \mathbf{b}^{ij} denotes the outward normal vector, the outward normal of the edge j with the norm being equal to the length of this edge. For the meso-loop i with s edges, the average velocity gradient tensor \bar{L}^i is expressed as below,

$$\bar{L}^i = \frac{1}{6A^i} \sum_{j_1, j_2 \in \{0, 1, \dots, s\}} Q_{j_1, j_2}^s \hat{v}^{ij_1} \otimes \mathbf{b}^{ij_2}, \tag{1}$$

where A^i is the area of the meso-loop i , “ \otimes ” is the dyadic product operator, and Q_{j_1, j_2}^s is the multiplier given according to the number of edge s , which has been exactly defined by Kuhn [28]. The symmetric part of \bar{L}^i gives the average strain rate tensor for meso-loop i

$$\bar{\epsilon}^i = \frac{1}{2} (\bar{L}^i + \bar{L}^{i^T}), \tag{2}$$

where \bar{L}^{i^T} is the transposition of \bar{L}^i .

Table 2 Specimens and corresponding initial void ratio

Specimens	e_0
S1	0.151
S2	0.179

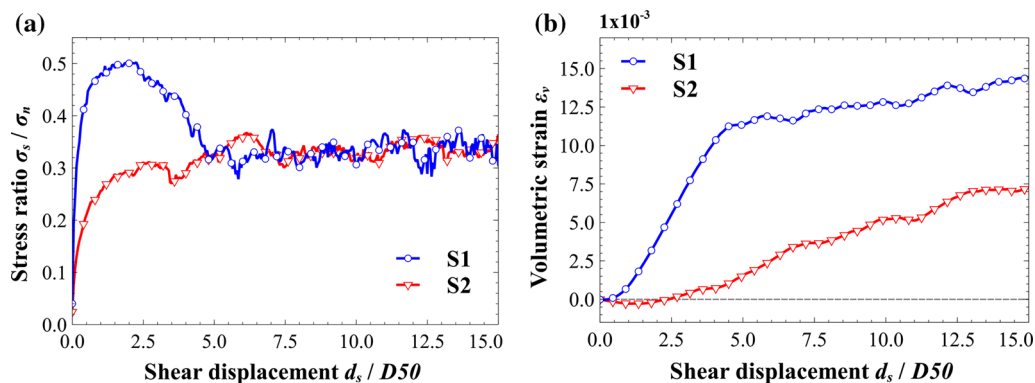


Fig. 2 **a** Stress ratio σ_s/σ_n and **b** volumetric strain ϵ_v with respect of shear displacement $d_s/D50$

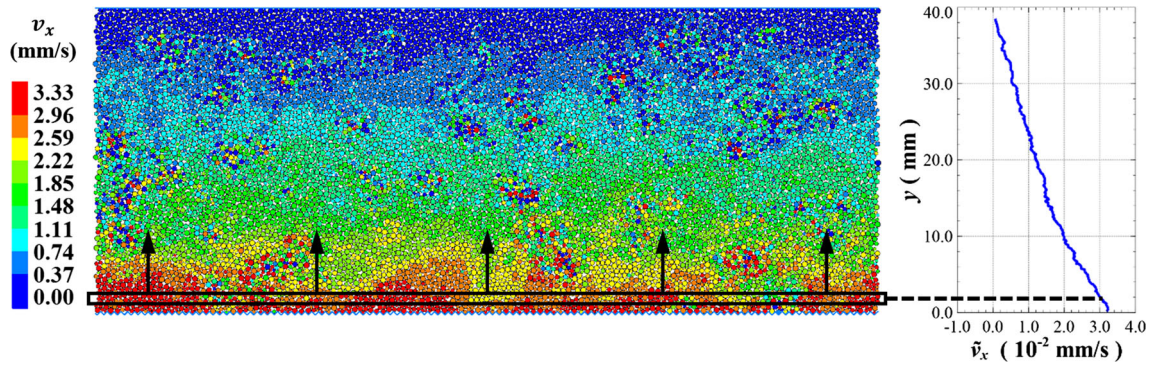


Fig. 3 Schematic diagram of measuring \bar{v}_x by the moving average scheme. On the *left* is the specimen S1 at $d_s/D_{50} = 0.5$ with particles colored according to the magnitude of v_x . On the *right* is the line chart of measured \bar{v}_x as function of y (color figure online)

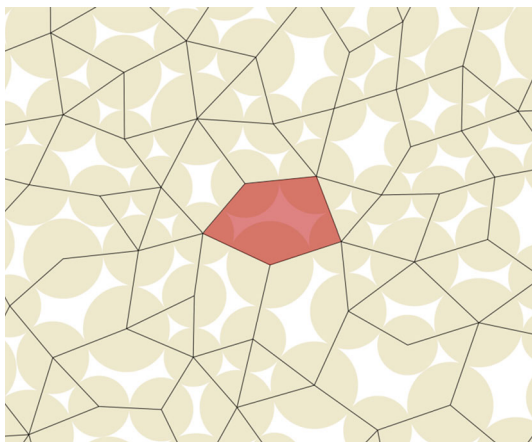


Fig. 4 Meso-loops enclosed by contacts represented by *black branches*

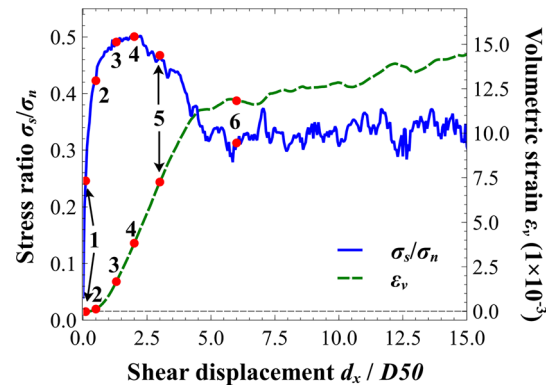


Fig. 6 For S1 stress ratio σ_s/σ_n and volumetric strain ϵ_v with respect to shear displacement d_s/D_{50} , with 6 monitoring strain states labeled by red points: $d_s/D_{50} = 0.10, 0.50, 1.30, 2.00, 3.00,$ and 6.00 (color figure online)

4 Formation of localized band

The strain localization process will be studied in this section. The velocity field and its gradient field will be explored in an attempt to capture the featured evolutionary patterns in the development of strain localization and localized band formation.

4.1 Evolution of shear velocity field

We plot the average horizontal velocity $\bar{v}_x(y)$ for the dense specimen S1 in Fig. 7, at 6 chosen strain states: d_s/D_{50} is, respectively, equal to 0.10, 0.50, 1.30, 2.00, 3.00 and 6.00, as labeled in Fig. 6.

For specimen S1, $\bar{v}_x(y)$ keeps in quasi-linearity at the early stage of the test (corresponding to strain state 1 and 2 in Fig. 6) when the specimen is believed to be in the elastic regime. $\bar{v}_x(y)$ is observed to bend from the downside at state 3, somewhere in the stress-hardening regime. It is followed by an obvious deflection on $\bar{v}_x(y)$ at state 4, a

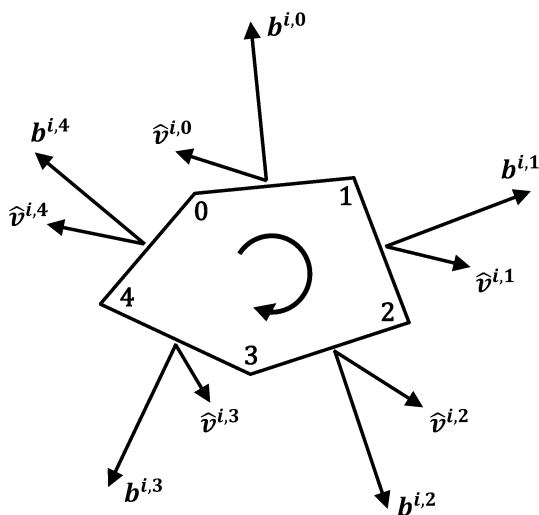


Fig. 5 For the edge j in the meso-loop i , the outward normal vector $b^{i,j}$ and the relative velocity vector $\hat{v}^{i,j}$

state approaching the stress peak. When the nonlinearity of $\tilde{v}_x(y)$ develops to state 5 at the stress softening, shear deformation concentrates on the bottom of the specimen, that is, large-scale strain localization. At the stress steady state (e.g., at state 6), the shear deformation almost completely localizes into the zone above the rough surface while vanishing outside this zone. This phenomenon signals a stable pattern in the strain localization. In other words, a steady localized band has been formed.

The average horizontal velocity $\tilde{v}_x(y)$ for the loose specimen S2 is plotted in Fig. 9, at 6 chosen strain states: $d_s/D_{50} = 0.20, 1.00, 3.40, 6.00, 7.05$ and 9.75 , as labeled in Fig. 8.

In the stress-hardening phase of S2, the nonlinearity of $\tilde{v}_x(y)$ is observed to develop from state 1 (corresponding to Fig. 9a) to the state 3 (Fig. 9c). At state 3, a pronounced deflection of $\tilde{v}_x(y)$ occurs in the lower part of the sample with a small drop in the stress. The strain localization seems to evolve to its steady form from state 3 onward. However, it is followed by a straight shaped $\tilde{v}_x(y)$ at state 4 (Fig. 9d). In other words, the non-affine deformational pattern recovers to an affine one. The nonlinearity reappears in $\tilde{v}_x(y)$ at state 5 (Fig. 9e) and maintains to state 6 (Fig. 9f).

It is concluded that the strong strain localization has shaped in both S1 and S2, as the velocity field is stratified into two phases (as illustrated in Fig. 7e): the nonlinear phase covering the surface and the linear phase in the remaining part of the sample. Moreover, the evolution of the velocity field in the loose sample is quite different from in the dense one. The nonlinear manner of $\tilde{v}_x(y)$ can persist to the end of the test once it appears in the dense specimen but has been observed to vanish and reappear in the loose specimen.

Generally, with the help of $\tilde{v}_x(y)$, the velocity field of specimens is visualized in such a simple way that its non-affinity can be clearly manifested and easily noted. However, $\tilde{v}_x(y)$ only displays the profile of the specimen's kinematics at some individual strain states. The evolution of the kinematic field of samples should be investigated in more detail. A continuous and quantitative characterization of the strain localization is required and will be solved in the following subsection.

4.2 Development of strain localization

A new indicator α is proposed to quantitatively characterize the degree of strain localization along the loading path. As illustrated in Fig. 10, $\tilde{v}_x(y)$ can be linearly approximated based on the boundaries' movement so that the approximation function $v_x^l(y)$ is equal to the boundaries' velocity at the depths of top and bottom boundaries: $v_x^l(0.0) = 3.33$ mm/s; $v_x^l(4.0) = 0.00$ mm/s. Of note, due to the high friction attributed to contacts between boundaries and

grains, there are $\tilde{v}_x(0.0) \approx v_x^l(0.0)$ and $\tilde{v}_x(4.0) \approx v_x^l(4.0)$. An error exists in this approximation due to the nonlinearity of $\tilde{v}_x(y)$. Integrating this error over y gives the total error:

$$S_{\text{err}} = \int_{0.0}^{4.0} |v_x^l - \tilde{v}_x| dy, \quad (3)$$

and α is defined as the normalized error:

$$\alpha = \frac{S_{\text{error}}}{S_{\text{linear}}} = \frac{\int_{0.0}^{4.0} |v_x^l - \tilde{v}_x| dy}{\int_{0.0}^{4.0} v_x^l dy}. \quad (4)$$

A larger α corresponds to a larger error in the approximation due to the nonlinearity of $\tilde{v}_x(y)$ and therefore corresponds to a larger degree of strain localization. It is worth mentioning that there is always difficulty in terms of describing the strain localization through analyzing the kinematic field of the material. Most of literatures present scenes of displacement or strain fields at individual strain states, which merely provide a qualitative overview on the concentrated strain. Otherwise, it is almost impossible to use a function to fit the measured velocity field, as a normal function is insufficient to contain the enrichment of presented patterns in the strain localization of the interface shearing (such as those shown in Figs. 7, 9). This proposed indicator allows the strain localization to be quantified into a scatter so that its evolution can be conveniently traced during shearing. In Fig. 11, we plot the evolution of α during the loading history for S1 and S2 and compare it with evolutions of the stress and volumetric strain. We notice that α for S2 is displayed until $d_s/D_{50} = 20.0$.

In dense specimen S1 (shown in Fig. 11a, b), α steadily ascends during the stress-hardening regime. This scene absolutely changes with a dramatic increase of α from a characteristic point close to but before the stress peak. Strain localization promptly develops afterward until the stress steady state is reached, and α keeps fluctuating at a high level, around 0.85. This result refers to the considerable development of nonlinearity in $\tilde{v}_x(y)$ from strain state 4 to 5 (shown in Fig. 7d and e, respectively).

In loose specimen S2 (Fig. 11c, d), α evolves with violent oscillation in a chaotic pattern. Both high and low values of α have temporarily emerged during the loading history. Generally viewing the curve of α , we note a big valley around in the range $d_s/D_{50} \in [5.00, 7.00]$. In this valley, α dramatically drops from a high value (close to 8.0) to vanish at strain state 4 and transiently increases afterward to touch the original level of α . This result is corroborated by the characteristic transformation of $\tilde{v}_x(y)$ along states 4, 5, and 6 (shown in Fig. 9c, d, and e, respectively), that is, the transition from a highly nonlinear

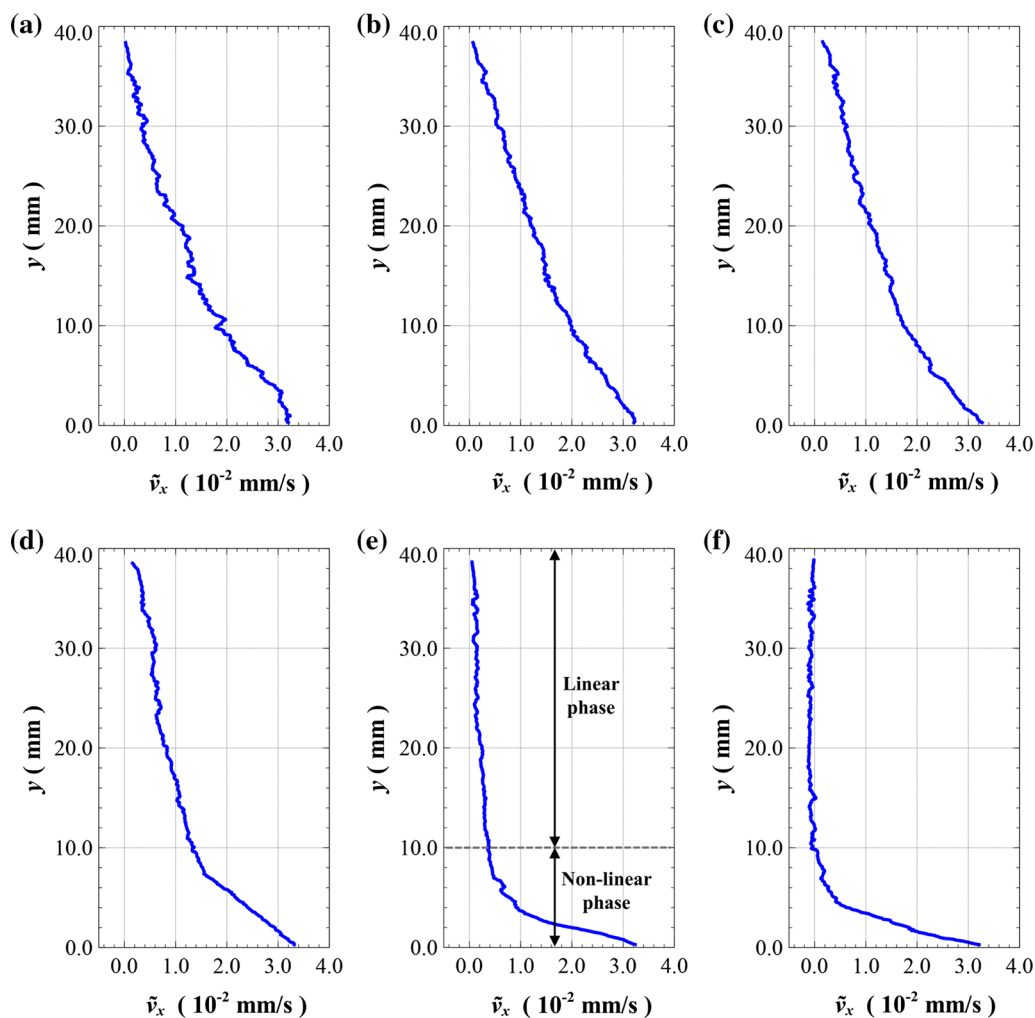


Fig. 7 For S1 distribution of average horizontal velocity \tilde{v}_x in terms of y at strain states **a** 1, **b** 2, **c** 3, **d** 4, **e** 5, and **f** 6. In (e) the linear and nonlinear phases of $\tilde{v}_x(y)$ are marked

curve of $\tilde{v}_x(y)$ to a quasi-linear one and the recovery to the original pattern. Moreover, such an unsteady pattern in the strain localization can also be captured after state 6, during $d_s/D_{50} \in [10.55, 13.15]$ and $[14.30, 19.70]$, as highlighted by transparent blue in Fig. 11d. Otherwise, after the specimen reaches the stress steady state (considered as $d_s/D_{50} > 5.0$ in S2), the dilatancy rate is found to be notably relevant to α ; a lighter strain localization, with a lower α , basically corresponds to a higher dilatancy rate.

4.3 Evolution of shear velocity gradient

To elucidate the evolution of the spatial distribution of the shear deformation in the granular assembly, the gradient of the shear velocity \bar{L}_{12}^i ($i = 1, 2, \dots, N_l$) is plotted for S1 in Fig. 12 and for S2 in Fig. 13, at measuring strain states already labeled in Figs. 6 and 8. The negative value of \bar{L}_{12}^i , colored by blue (or positive value colored by red) represents the shear deformation along (or against) the subjected

shear load of the specimen. It is noteworthy that instead of using the shear strain rate $\dot{\epsilon}_{12}^i$, which is equal to $\frac{1}{2}(\bar{L}_{12}^i + \bar{L}_{21}^i)$, we chose to display \bar{L}_{12}^i , the gradient of the shear velocity in terms of the vertical direction. By doing so, the shear deformation along different depths of the specimen can be clearly manifested.

In the dense specimen, the deformation is more or less homogeneous at state 1 (Fig. 12a) in the very early stage of the test. Despite this outcome, some small-scale deformational concentrations have been found to already exist, arranging along the shear direction, preferentially at the bottom of the specimen. With the expansion and conjugation among these tiny strain concentrations, the deformation appears to be discontinuous at the onset of stress hardening, around state 2 (Fig. 12b), even though no pronounced rupture exists in the material. To state 3 (Fig. 12c), several readily perceivable bands have formed: one clearly at the bottom and two blurrily on the top and in the middle of the sample, respectively, as marked inside the

ellipses in Fig. 12c. The bottom band of the strain localization becomes clearer and paramount over the specimen near the stress peak, as shown in Fig. 12d. In the following

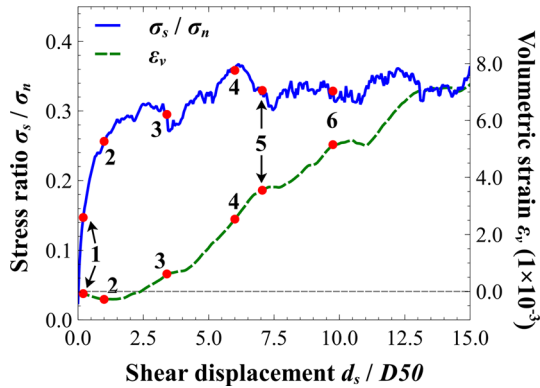


Fig. 8 For S2 stress ratio σ_s/σ_n and volumetric strain ϵ_v with respect of shear displacement d_s/D_{50} , with 6 monitoring strain states labeled by red points: $d_s/D_{50} = 0.20, 1.00, 3.40, 6.00, 7.05,$ and 9.75 (color figure online)

stress-softening regime, the strain acceleratingly localizes into the downside of the specimen. A notable localized band promptly shapes above the rough surface, as the shear deformation sufficiently concentrates inside the localized band and almost vanishes outside it. Meanwhile, the positive value of \bar{L}_{12}^i , which is in red, is observed somewhere outside the localized band, referring to the unloading of the material.

At state 1 (Fig. 13a) of the loose specimen, there is a generally homogeneous order in the distribution of \bar{L}_{12}^i , accompanied by many trivial local failures (or small-scale strain localizations) diffusing over the specimen. The unloading of the material is noted in areas (of red) alongside these failures. We call this pattern hereafter the diffuse failure mode. It is noteworthy that when also believed to be generally homogeneous, the diffuse failure mode involves local strain localizations on a larger degree and scale than those beheld at state 1 of S1 (referring to Fig. 13a). Between strain states 2 and 3 (Fig. 13b, c), the specimen experiences a gradual strain localization into the sample’s

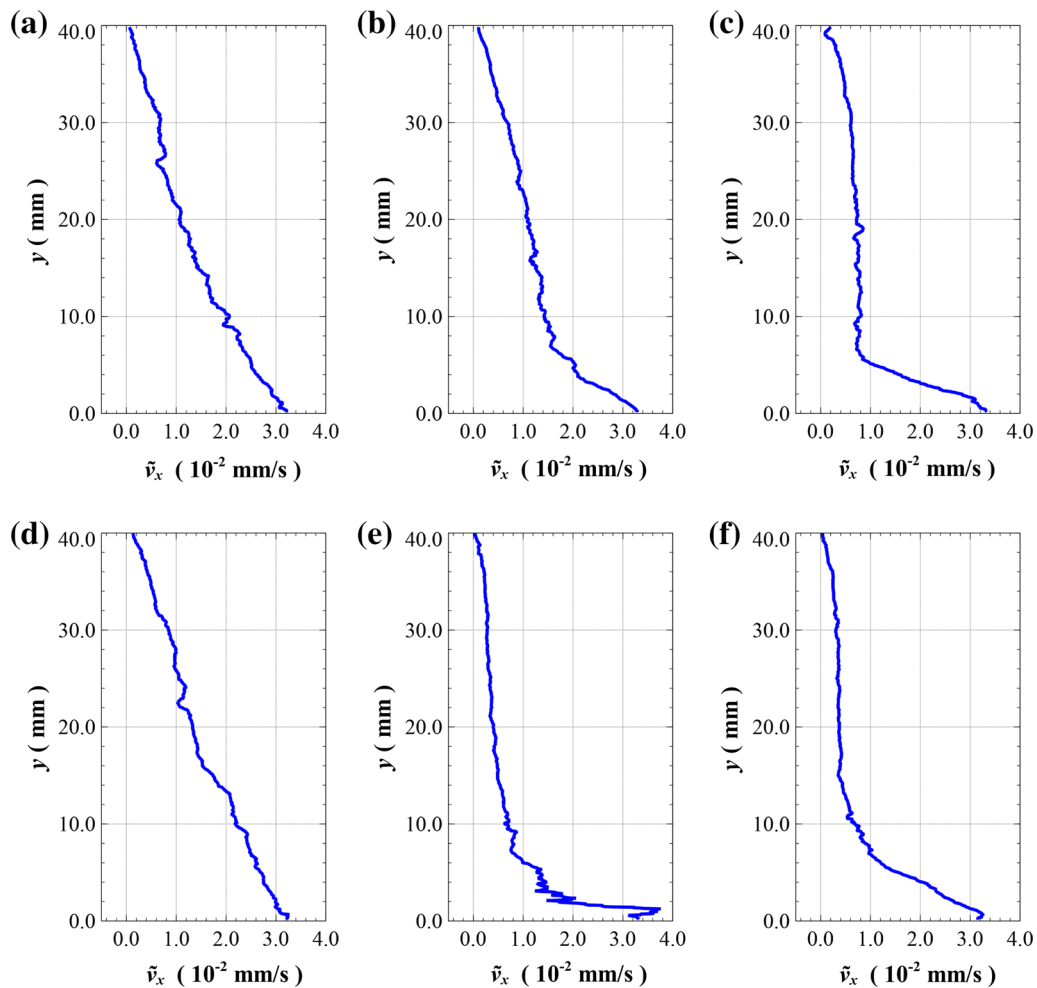


Fig. 9 For S2 distribution of average horizontal velocity \bar{v}_x in terms of y at strain states **a** 1, **b** 2, **c** 3, **d** 4, **e** 5, and **f** 6

bottom and an unload of the material elsewhere. This failure mode is designated as the localized failure mode. At state 4, as previewed in the velocity field (referring to Fig. 9d), the velocity gradient field displays a scene reminiscent of that presented in state 1. Failures resume diffusion in the material after shortly being localized. However, this pattern still cannot be sustainable. Diffuse failures disappear afterward and turn into an increasingly localized

failure, as shown in Fig. 13e and f for state 5 and state 6, respectively. This is similar to what has happened from state 1 to 3, that is, the appearing and strengthening of the localized failure from a generally homogeneous deformation with diffuse failures.

4.4 Particle rotation

Particle rotation plays significant role in the formation of the localized band [1, 3, 24, 25, 32]. The magnitude of rotation $|\theta|$ on particles is plotted at 4 respective monitoring strain states in Fig. 14 for S1 and in Fig. 15 for S2. Clockwise and counterclockwise rotations herein are not distinguished.

The spatial distribution of $|\theta|$ follows the way \bar{L}_{12}^i evolves in both specimens, as the particle rotation concentrates in the area in which the shear deformation localizes. There is a pronounced association between particle rotation and strain localization. In S1, $|\theta|$ gradually stresses to form a distinct and continuous area with a high level of particle rotation running through the bottom of the specimen. In S2, $|\theta|$ tends to localize from state 2 to 3, resumes to be seemingly homogeneous at state 4, and localizes again at state 6. Otherwise, $|\theta|$ in S2 is generally smaller and less concentrated than that in S1.

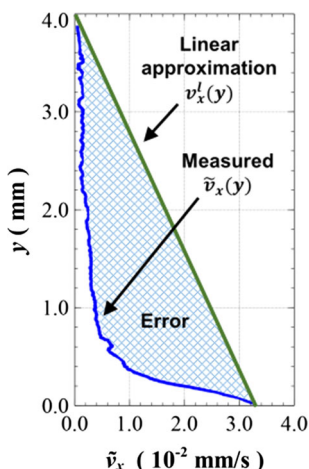


Fig. 10 In terms of y , average velocity \bar{v}_x , its linear approximation v_x^l calculated from the boundary movement and the error $|v_x^l - \bar{v}_x|$

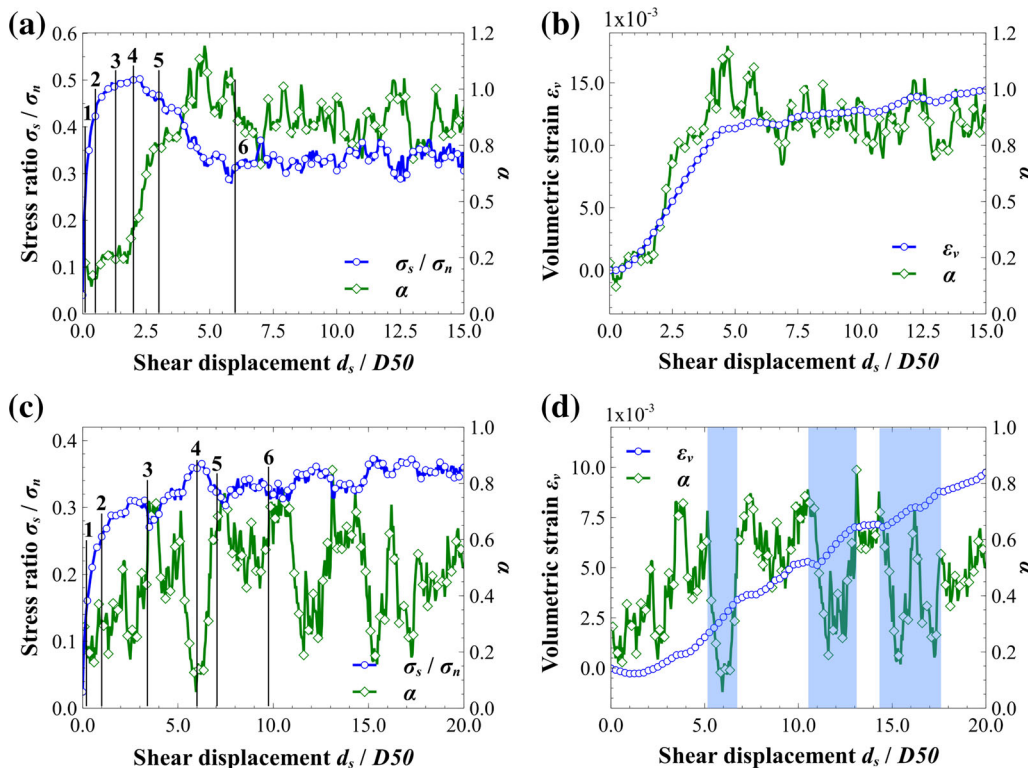


Fig. 11 With respect to shear displacement d_s/D_{50} , evolutions of α , compared with evolution of σ_s/σ_n for **a** S1 and **c** S2, and with evolutions of ϵ_v for **b** S1 and **d** S2. Monitoring strain states referred to in Figs. 6 and 8 for S1 and S2, respectively, are also labeled in (a) and (c)

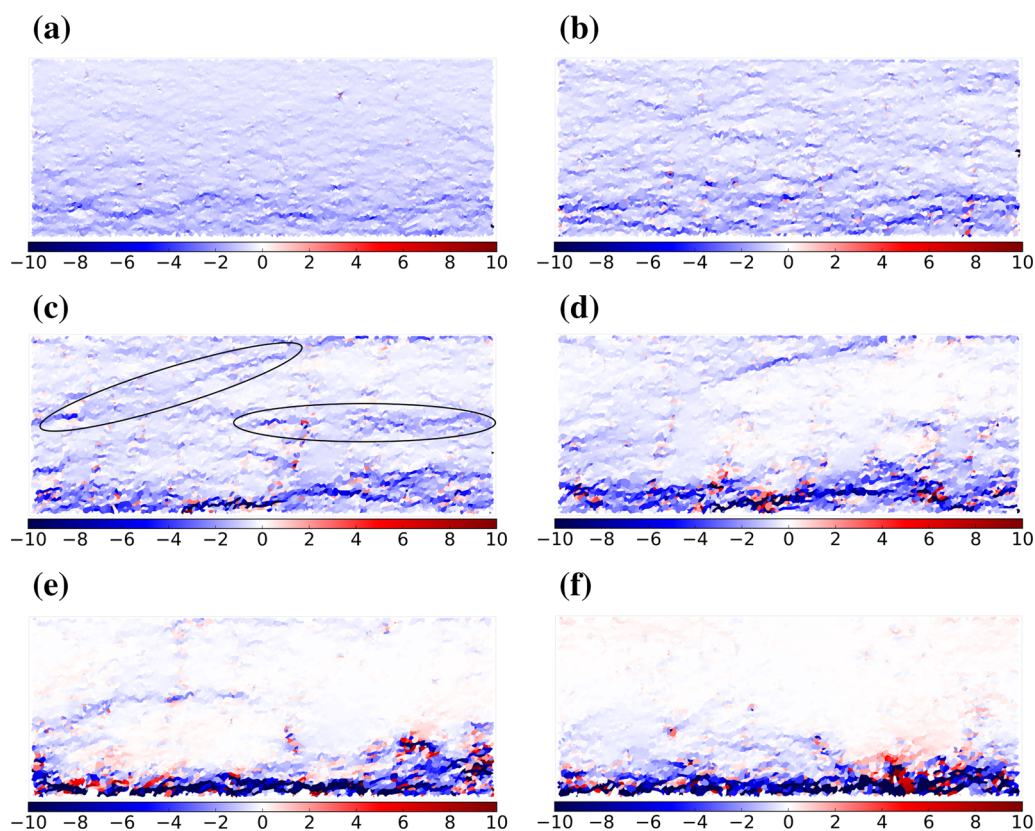


Fig. 12 For S1, distribution of \bar{L}_{12}^i (10^{-3} s^{-1}) at strain states **a** 1, **b** 2, **c** 3, **d** 4, **e** 5, and **f** 6

5 Discussion

Generally, developments of $\bar{v}_x(y)$, α , and \bar{L}_{12}^i are consistent with each other and can be mutually supported during the loading history of both S1 and S2. In these two specimens, the localized band has been observed to be shaped on the bottom of them, featured by considerable and sufficient strain localizations into a band-like area. In particular, several characteristic trends were presented, which will be discussed in the following paragraphs.

5.1 Dense specimen S1

As shown in Fig. 12a, tiny deformational concentrations have already existed at the fairly small strain, especially in the soil downside the specimen, indicating that the deformation was structured even from the very early stage of the shearing. With the progress of the shear deformation, these local deformational heterogeneities in the small scale grow, elongate, and conjugate with each other afterward, leading to an escalating degree of strain localization. This result is also reflected in Fig. 11a by a jolting upward trend of α in elastic and stress-hardening regimes. Near the end of the stress hardening, the deformation has been sufficiently localized into several band-shaped areas. This is followed

by a characteristic moment, prior to the stress peak, with an abrupt uprising of α , when the strain largely localizes at the bottom of the specimen and vanishes elsewhere. During the subsequent stress-softening regime, a distinct pattern appears and is promptly strengthened, along with a mounting deformational concentration, indicating the formation of the localized band, which can persist to the end of the test.

Tiny concentrations of the shear deformation found at the very early stage of the test are reminiscent of what was noticed by Kuhn [28] in the drained biaxial test. In the study, micro-bands, characterized by a higher slip deformation than their vicinities, were observed to prevail over the specimen even at a very small shear strain. These micro-bands are composed of several particles in thickness and tens of particles in length. The shear deformation proves to be locally heterogeneous since it is at a very low level. However, how the large-scale strain localization is developed from the expanding, bridging, and merging of these local patterns should be explained in more detail.

In this study, potential bands with a high deformational concentration were observed to emerge before the stress peak and develop toward one steady localized band during the stress-softening regime. This observation was also reported by Gu et al. [16] in the numerical drained biaxial

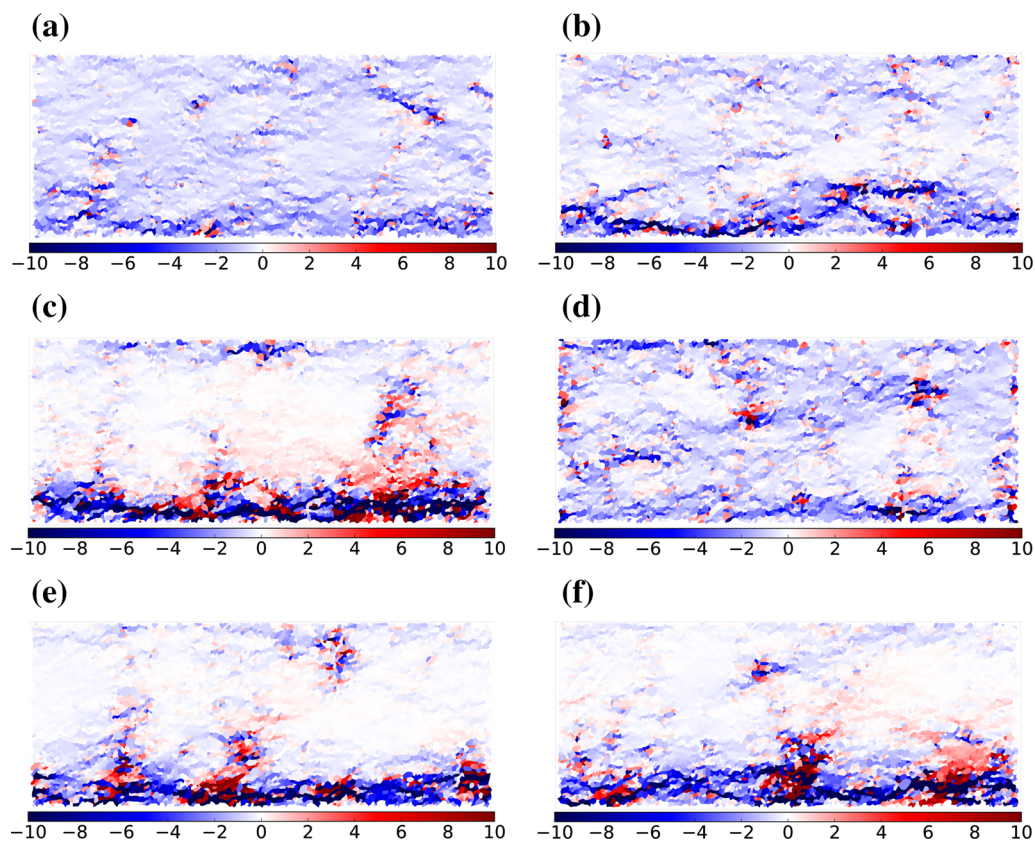


Fig. 13 For S2, distribution of \bar{L}_{12}^i (10^{-3} s^{-1}) at strain states **a** 1, **b** 2, **c** 3, **d** 4, **e** 5, and **f** 6

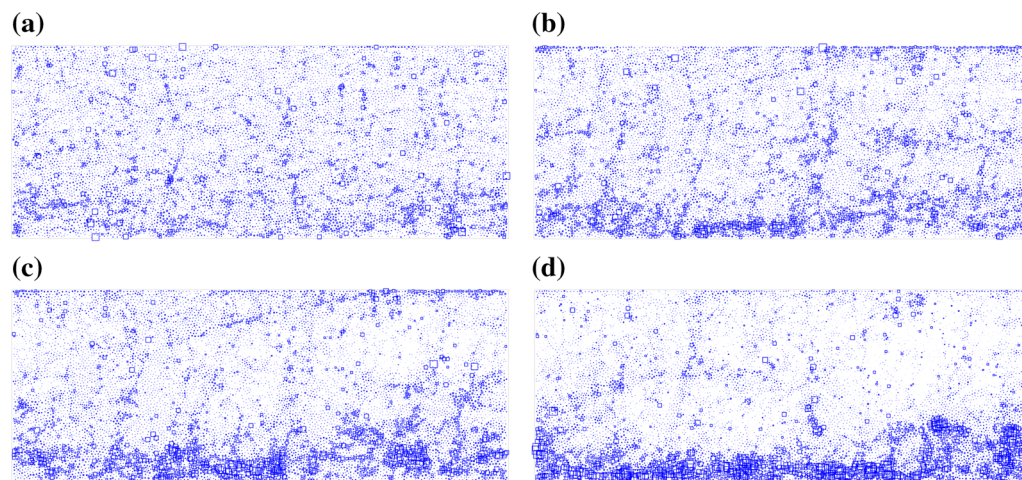


Fig. 14 Distribution of $|\theta|$ for S1 at strain states **a** 2, **b** 3, **c** 4, and **d** 5. The *square's size* is proportional to the magnitude of the particle rotation

test. In fact, the formation of localized band refers to a bifurcation from a homogeneous deformation toward a discontinuous one [31]. A number of possible deformational patterns hold at the onset of this bifurcation, resulting in diversified post-bifurcation states [22]. To this extent, the emergence of potential bands signals the arrival of the bifurcation process and gives rise to the diverse

mechanical performance of SSI in the post-bifurcation section.

5.2 Loose specimen S2

The spatial distribution of the shear deformation in the loose specimen evolves in a significantly different

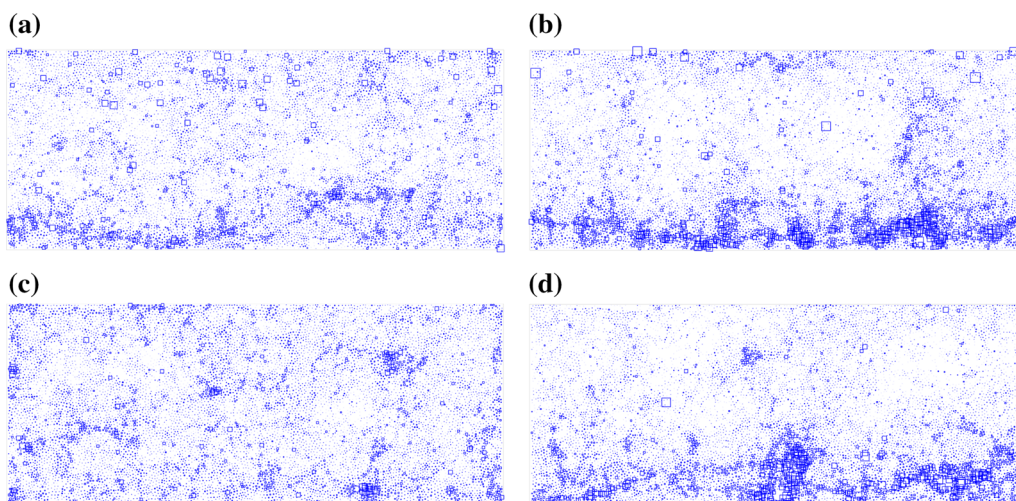


Fig. 15 Distribution of $|\theta|$ for S2 at strain states **a** 2, **b** 3, **c** 4 and **d** 6. The *square's* size is proportional to the magnitude of the particle rotation

Table 3 Two complementary loose specimens and corresponding initial void ratios

Specimens	e_0
S21	0.179
S22	0.181

manner from that in the dense specimen, even though the localized pattern was beheld in both of them. Failures in localized and diffuse modes are observed to appear alternatively during the loading history. As far as the end of the test ($d_s/D_{50} = 20.0$), the granular system of S2 has not deformed into a steady localized pattern. All experienced large-scale localized deformation can be only temporary and variable, contrary to the localized band in the dense specimen, which can persist to the end of the test once it appears. For those who may argue against the representativeness of S2’s mechanical preformation, we add two complementary loose specimens listed in Table 3, which are also installed and sheared according to parameters listed in Table 1. Evolutions of σ_s/σ_n , ε_v , and α for these two additional specimens S21 and S22 are demonstrated in Fig. 16. Similar to what is observed for S2, these two additional specimens present chaotic variations of α ; transitions between the highly localized pattern and the generally homogeneous one, like those observed in S2, also exist in specimens S21 and S22, at the sections highlighted in the transparent blue in Fig. 16b and d.

It is concluded that a steady localized band may not arise at the large strain in the loosely assembled granular soil subjected to the interface shearing. Considering this case, the determined band area at a strain state will be invalid in another state. In particular, when the granular material undergoes the diffuse failure mode, it is

impossible to distinguish a clear zone containing sufficiently localized deformation. The featured deformational mechanism for the loose sample will be discussed in more detail in the next subsection.

It is worth mentioning that the evolutionary localized banding and its final pattern in SSI are appreciably constrained by the system’s intrinsic boundary condition. In this study, the periodic boundary condition (PBC) is assigned to simulate the nature of the SSI system with an (equivalently) infinite length along the shear direction. However, the diffuse failure mode captured in the PBC will not appear in the conventional interface shear test with the displacement boundary condition (DBC) on both sides, in which two fix boundaries are configured at both side of the sample. For the lower part of the granular assembly S at a depth of h , as illustrated in Fig. 17, $\bar{\sigma}_s(h)$ denotes the subjected average shear stress on the top of S , $\bar{F}_1(h)$ and $\bar{F}_2(h)$ are the total forces applied on the left and the right boundaries of S , respectively, and $\sigma_{n,1}(y)$ and $\sigma_{n,2}(y)$ denote the normal stress distributed on the left and the right boundaries, respectively, in terms of y . Considering the equilibrium of S along the direction of the shear load gives

$$\bar{\sigma}_s(h) - \sigma_s = \frac{\bar{F}_1(h) - \bar{F}_2(h)}{w} = \frac{1}{w} \int_0^h (\sigma_{n,1}(y) - \sigma_{n,2}(y)) dy. \tag{5}$$

In case of the PBC, Newton’s third law in terms of each interaction across the periodic boundary ensures equaling between $\bar{F}_1(h)$ and $\bar{F}_2(h)$, and vanishing of the item $\frac{\bar{F}_1(h) - \bar{F}_2(h)}{w}$. $\bar{\sigma}_s(h)$ with PBC is therefore constant, being equal to σ_s . With the DBC of fixed side boundaries, due to the moving trend of mass toward the right boundary, arguably, $\sigma_{n,2}(y)$ is larger than $\sigma_{n,1}(y)$ for various y . This

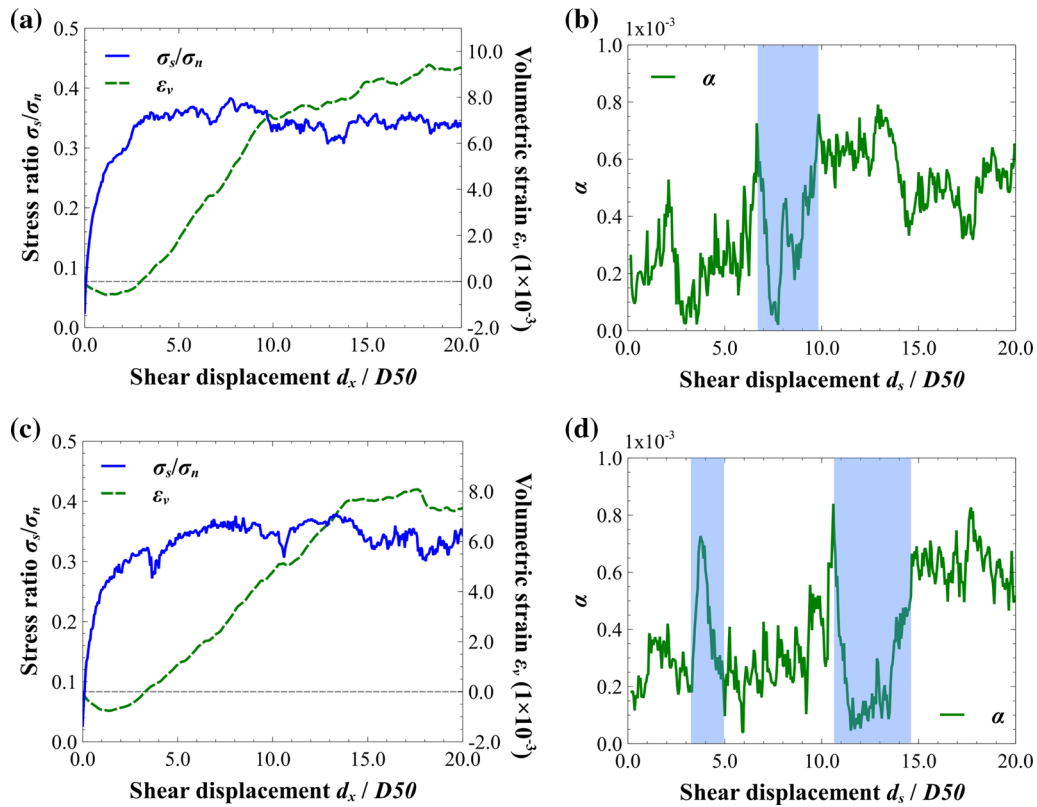


Fig. 16 With respect to shear displacement d_s/D_{50} , evolutions of σ_s/σ_n , and ϵ_v for **a** S21 and **c** S22 and evolutions of α for **b** S21 and **d** S22

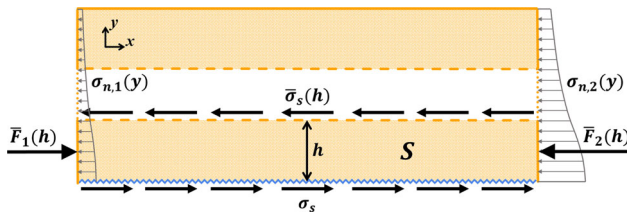


Fig. 17 Subjected forces and the equilibrium of a lower part of the granular assembly S along the shear direction

Table 4 Four complementary specimens and S1 and S2 with their corresponding initial void ratios

Specimens	e_0
S1	0.151
S11	0.157
S12	0.166
S13	0.171
S14	0.175
S2	0.181

results in an increasing negativity of $\bar{\sigma}_s - \sigma_s$ with the increasing h , that is, the reduction of $\bar{\sigma}_s$ with increasing depth. In consequence, the shear strain can concentrate nowhere but on the downside of the specimen. To this

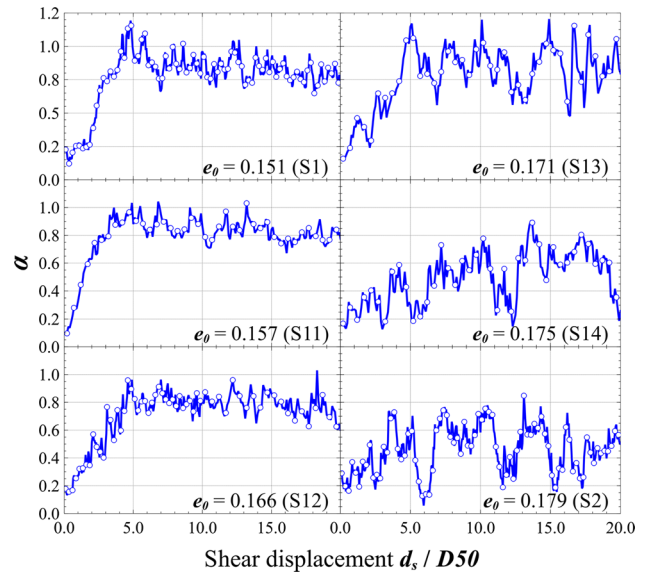


Fig. 18 Evolutions of α for S1 (dense specimen), S11, S12, S13, S14, and S2 (loose specimen) with respect to shear displacement d_s/D_{50}

extent, the interface shear test with fix side boundaries is probably unable to produce a sensible stress and deformational mechanisms for SSI with an equivalently infinite length in the shear direction.

5.3 Patterns transition between dense and loose specimens

The strain localization presents distinct pattern in loose specimen from that in the dense specimen. Why the pattern differs according to the initial void ratio remains not answered. Finding transitional patterns between these two distinct ones might shed light on understanding the underlying mechanism. Four complementary specimens with intermediate initial void ratios between the dense and loose specimens (listed and labeled in Table 4) are prepared and loaded according to parameters listed in Table 1. Evolutions of α for four additional specimens (S11, S12, S13, and S14) and S1 and S2 are shown in Fig. 18. We also statistically account final values of α ($7.5 \leq d_s/D_{50} \leq 20$) for all specimens in Fig. 19, in which for each specimen a bar represents the statistical estimation of α for its standard deviation (upper and lower bonds), median (middle line), and mean value (red cross).

Generally, a denser specimen tends to reach a higher level of α (with an increasing median and mean value), and a looser specimen tends to display a more unstable and fluctuating α (with a higher standard deviation). Strain localizations in first four specimens (S1, S11, S12, and S13) escalate during $d_s/D_{50} = [0.0, 5.0]$ to high levels and fluctuate around them thereafter, whereas loose specimens S14 and S2 present more chaotic paths of α , which abruptly

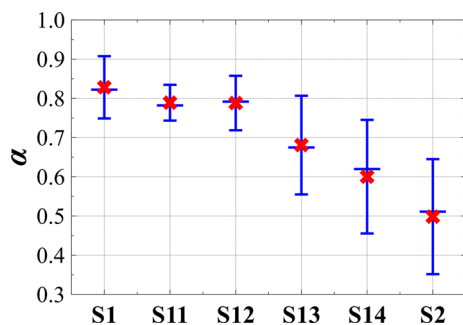


Fig. 19 Statistical quantities of α during $7.5 \leq d_s/D_{50} \leq 20$ for S1, S11, S12, S13, S14, and S2: standard deviation (upper and lower bonds), median (middle line), and mean value (red cross) (color figure online)

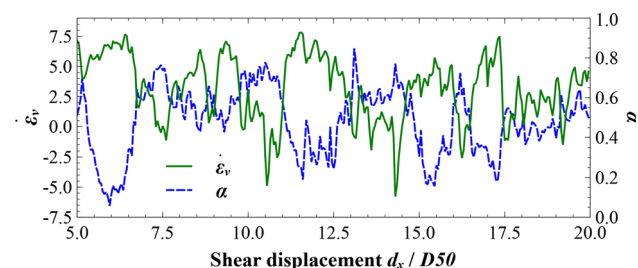


Fig. 20 $\dot{\epsilon}_v$ and α with respect to d_s/D_{50} in S2 during $d_s/D_{50} \in [5.0, 20.0]$

alternate between high and lower values. A critical sign is captured in Fig. 18 in S13 (a center-loose specimen) as strong vibration occurs after peak, indicating that the specimen seems unable to maintain the high level of α . This is shown more conspicuously in Fig. 19 that the standard deviation prominently grows from S12 to S13. Two looser specimens than S13 are dominated by too strong vibrations (with large standard deviations) to see any clear pattern.

The chaotic strain localization path proves to be a common behavior of loosely packed granular soil. The soil initialized with lower density is less competent to maintain a high level of strain localization. A reasonable explanation is that due to the low density and weak force-chains in loose soil, the granular system outside localized band is not stable enough to maintain its long-term intactness under the load and disturbance transmitted from the localized band area. When divergence also occurs in the outside localized band area, the global situation for a high degree of strain localization loses. This is then followed by a less localized pattern, with which the potential energy cumulates in the whole material, waiting for the next term of localized banding.

5.4 Volumetric evolution versus strain localization

Figure 11d shows that after the stress steady state is reached in S2 (more or less at $d_s/D_{50} = 5.0$), the strain localization is highly related to the dilatancy of the material. Evolutions of the global volumetric strain rate $\dot{\epsilon}_v$ and α of S2 are plotted in Fig. 20, showing a generally reverse trend between them. A lower degree of the strain localization corresponds to a higher dilatancy rate during the stress steady state. This result is supported by a highly negative correlation between $\dot{\epsilon}_v$ and α , measured by Pearson coefficient r ($r = -0.717$, as shown in Fig. 21b). The Pearson coefficient r , ranged in $[-1.0, 1.0]$, and its confident interval (CI) are given by the Pearson test to evaluate the linear correlation between two variables [33]. Reducing r from 1, through 0, to -1 refers to changing from the perfectly positive correlation, to no correlation, to the perfectly negative correlation. S1 also weakly exhibits this trend during the stress steady state, with $r = -0.577$ (Fig. 21a).

Previous research has reported that in a well-developed localized band, a singular and constant material fabric is developed with characteristic micro- and meso-structures [14, 57, 58], leading to a constant volume and shear strength of the material. Thus, there must finally be dynamical equilibrium between the local contractancy and local dilatancy inside the localized band, which has well developed during the stress steady state. The global volumetric evolution during the stress steady state, to this extent, turns to attribute to the shear-dilatancy nature of the

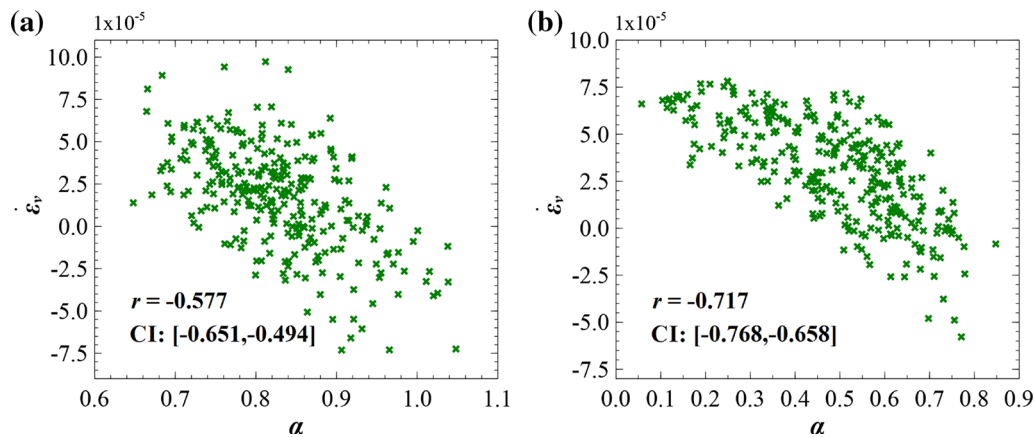


Fig. 21 $\dot{\epsilon}_v$ versus α **a** for S1 during $d_s/D_{50} \in [6.0, 20.0]$ and **b** for S2 during $d_s/D_{50} \in [5.0, 20.0]$. Pearson correlation r and its confidence interval CI with 95% confidence level

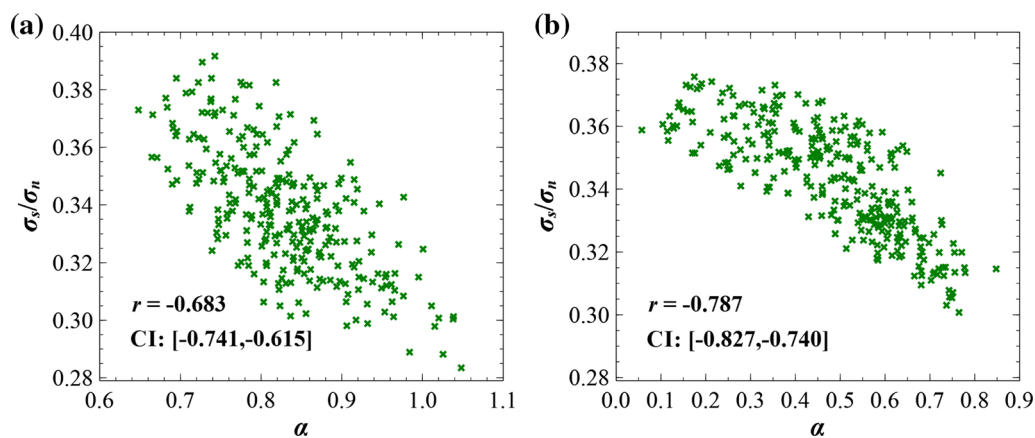


Fig. 22 σ_s/σ_n versus α **a** for S1 during $d_s/D_{50} \in [6.0, 20.0]$ and **b** for S2 during $d_s/D_{50} \in [5.0, 20.0]$. Pearson correlation r and its 95% confidence interval (CI)

material outside the localized band. A degradation of the strain localization, corresponding to an increasing shear strain imposed on the outside localized band area, will lead to a higher dilatancy rate of the soil. This is likely the reason why there is a negative correlation between the degree of the strain localization and the dilatancy rate.

5.5 Shear strength versus strain localization

During the stress steady state of S1 and S2, α almost reverses the ways the stress evolves, as the stress softening (or hardening) corresponds to the increasingly (or decreasingly) localized deformation. The correlation between σ_s/σ_n and α is evaluated through the Pearson correlation r for S1 and S2 (shown in Fig. 22). Remarkably high correlations are found between them in both specimens.

In essence, strain localization basically refers to the material's failure. The strongly localized deformation can cause significant damage on the preexisted force-bearing

structures, the force-chains (column-like clusters of particles, which carry a major part of the external loading), thus leading to stress softening. Of note, the particles' rotation has been identified as a fundamental pattern in the movement and buckling of the force-chain network [25, 39]. As Sect. 4.4 revealed, strain localization also induces the localization of the particle rotation. Force-chains buckling and stress softening will naturally follow.

6 Conclusions

The development of strain localization and the strain localization process has been studied in densely and loosely packed granular soil subjected to interface shearing. By analyzing the kinematical field in specimens, how the strain localization evolves and how this evolution is related to the mechanical shearing responses of SSI have been explored on the basis of DEM simulation. Based on the velocity field given by grains' translational and

rotational velocities, several kinematic quantities are tested at the monitoring strain states of both specimens. They are the average shear velocity $\tilde{v}_x(y)$, the gradient of the shear velocity \tilde{L}_{12}^i , and the spatial distribution of particle rotation $|\theta|$. By measuring the nonlinearity of $\tilde{v}_x(y)$, an indicator α is proposed to quantify the degree of the strain localization along the loading path. Main conclusions are summarized as follows:

1. According to $\tilde{v}_x(y)$ in dense and loose specimens, the velocity field at strain states with a strong strain localization has structured into two phases: the nonlinear phase covering the rough surface and the linear phase in the remaining part. The linear phase vanishes after the localized deformation has been sufficiently developed. The SSI system then can be essentially seen as the combination of the rough surface and the soil nearby with a highly nonlinear velocity field.
2. For the dense specimen, tiny deformational concentrations have been observed at the very early stage of the shearing. The level of strain localization steadily ascends during the stress-hardening regime. To a strain state prior to the stress peak, shear deformation has largely concentrated at several areas, preferentially at the specimen's bottom. During the stress-softening phase, one of the former shear concentrated areas becomes dominant, while the remainders gradually disappear. For the loose specimen, there is a chaotic evolution to strain localization. According to the evolution of α and \tilde{L}_{12}^i , a steady localized band has not arisen at the large strain, as the deformation pattern transforms between localized and diffused failure modes.
3. During the stress steady state, the degree of strain localization is highly associated with the strength and dilatancy of SSI. Besides, $|\theta|$ is found to stress at the concentrated area of the deformation, thus exhibiting a remarkably spatial association with the strain localization. The strongly localized deformation, accompanied by the high level of the particle rotation, will cause significant damage to the force-chains system and, subsequently, the stress softening.

Acknowledgements The authors gratefully acknowledge financial support from the Macau Science and Technology Development Fund (FDCT) 125/2014/A3, the National Natural Science Foundation of China (Grant No. 51508585), the University of Macau Research Fund MYRG2015-00112-FST and the Region Pays de la Loire of France (Project RI-ADAPTCLIM).

References

1. Bardet JP (1994) Special issue on microstructure and strain localization in geomaterials observations on the effects of particle rotations on the failure of idealized granular materials. *Mech Mater* 18:159–182. doi:10.1016/0167-6636(94)00006-9
2. Bardet J-P, Proubet J (1991) Numerical investigation of the structure of persistent shear bands in granular media. *Geotechnique* 41:599–613
3. Bardet J-P, Proubet J (1992) Shear-band analysis in idealized granular material. *J Eng Mech* 118:397–415
4. Bigoni D (2000) Bifurcation and instability of non-associative elastoplastic solids. Springer, Berlin
5. Chambon R, Caillerie D (1999) Existence and uniqueness theorems for boundaryvalue problems involving incrementally non linear models. *Int J Solids Struct* 36:5089–5099
6. Chareyre B, Villard P (2002) Discrete element modeling of curved geosynthetic anchorages with known macro-properties. In: *Proceedings of the first international PFC symposium*, pp 197–203
7. Cundall PA, Strack OD (1979) A discrete numerical model for granular assemblies. *Geotechnique* 29:47–65
8. Dejong JT, White DJ, Randolph MF (2006) Microscale observation and modeling of soil-structure interface behavior using particle image velocimetry. *Soils Found* 46:15–28
9. Desai CS, Drumm EC, Zaman MM (1985) Cyclic testing and modeling of interfaces. *J Geotech Eng* 111:793–815
10. Desrues J, Lanier J, Stutz P (1985) Localization of the deformation in tests on sand sample. *Eng Fract Mech* 21:909–921. doi:10.1016/0013-7944(85)90097-9
11. Desrues J, Chambon R, Mokni M, Mazerolle F (1996) Void ratio evolution inside shear bands in triaxial sand specimens studied by computed tomography. *Géotechnique* 46:529–546
12. Dove JE, Jarrett JB (2002) Behavior of Dilative Sand Interfaces in a Geotribology Framework. *J Geotech Geoenviron Eng* 128:25–37. doi:10.1061/(ASCE)1090-0241(2002)128:1(25)
13. Finno RJ, Harris WW, Mooney MA, Viggiani G (1997) Shear bands in plane strain compression of loose sand. *Geotechnique* 47:149–165
14. Fu P, Dafalias YF (2011) Fabric evolution within shear bands of granular materials and its relation to critical state theory. *Int J Numer Anal Methods Geomech* 35:1918–1948. doi:10.1002/nag.988
15. Gao Z, Zhao J (2013) Strain localization and fabric evolution in sand. *Int J Solids Struct* 50:3634–3648
16. Gu X, Huang M, Qian J (2014) Discrete element modeling of shear band in granular materials. *Theor Appl Fract Mech* 72:37–49. doi:10.1016/j.tafmec.2014.06.008
17. Guo N, Zhao J (2014) A coupled FEM/DEM approach for hierarchical multiscale modelling of granular media. *Int J Numer Methods Eng* 99:789–818
18. Guo N, Zhao J (2016) 3D multiscale modeling of strain localization in granular media. *Comput Geotech* 80:360–372
19. Guo N, Zhao J (2016) Parallel hierarchical multiscale modelling of hydro-mechanical problems for saturated granular soils. *Comput Methods Appl Mech Eng* 305:37–61
20. Guo N, Zhao J, Sun WC (2016) Multiscale analysis of shear failure of thick-walled hollow cylinder in dry sand. *Géotechnique Lett* 6:77–82. doi:10.1680/jgele.15.00149
21. Huang W, Bauer E, Sloan SW (2003) Behaviour of interfacial layer along granular soil-structure interfaces. *Struct Eng Mech* 15:315–329
22. Ikeda K, Yamakawa Y, Desrues J, Murota K (2008) Bifurcations to diversify geometrical patterns of shear bands on granular material. *Phys Rev Lett* 100:198001
23. Iwashita K, Oda M (1998) Rolling resistance at contacts in simulation of shear band development by DEM. *J Eng Mech* 124:285–292
24. Iwashita K, Oda M (1998) Shear band development in modified DEM: importance of couple stress. *TASK Q Sci Bull Acad Comput Cent Gdansk* 2:443–460

25. Iwashita K, Oda M (2000) Micro-deformation mechanism of shear banding process based on modified distinct element method. *Powder Technol* 109:192–205. doi:[10.1016/S0032-5910\(99\)00236-3](https://doi.org/10.1016/S0032-5910(99)00236-3)
26. Kishida H, Uesugi M (1987) Tests of the interface between sand and steel in the simple shear apparatus. *Géotechnique* 37:45–52. doi:[10.1680/geot.1987.37.1.45](https://doi.org/10.1680/geot.1987.37.1.45)
27. Kuhn MR (1997) *Deformation Measures for Granular Materials*. ASCE, pp 91–104
28. Kuhn MR (1999) Structured deformation in granular materials. *Mech Mater* 31:407–429
29. Lin J, Wu W, Borja RI (2015) Micropolar hypoplasticity for persistent shear band in heterogeneous granular materials. *Comput Methods Appl Mech Eng* 289:24–43
30. Mohamed A, Gutierrez M (2010) Comprehensive study of the effects of rolling resistance on the stress–strain and strain localization behavior of granular materials. *Granul Matter* 12:527–541
31. Nicot F, Darve F (2011) Diffuse and localized failure modes: two competing mechanisms. *Int J Numer Anal Methods Geomech* 35:586–601. doi:[10.1002/nag.912](https://doi.org/10.1002/nag.912)
32. Oda M, Kazama H (1998) Microstructure of shear bands and its relation to the mechanisms of dilatancy and failure of dense granular soils. *Geotechnique* 48:465–481
33. Pearson K (1895) Note on regression and inheritance in the case of two parents. *Proc R Soc Lond* 58:240–242
34. Petryk H (1993) *Theory of bifurcation and instability in time-independent plasticity*. Springer, Berlin
35. Stutz H, Mašín D, Wuttke F (2016) Enhancement of a hypoplastic model for granular soil–structure interface behaviour. *Acta Geotech* 11:1249–1261
36. Sulem J, Vardoulakis IG (2004) *Bifurcation analysis in geomechanics*. CRC Press, Boca Raton
37. Tejchman J, Górski J (2008) Deterministic and statistical size effect during shearing of granular layer within a micro-polar hypoplasticity. *Int J Numer Anal Methods Geomech* 32:81–107
38. Tejchman J, Wu W (1996) Numerical simulation of shear band formation with a hypoplastic constitutive model. *Comput Geotech* 18:71–84
39. Tordesillas A (2007) Force chain buckling, unjamming transitions and shear banding in dense granular assemblies. *Philos Mag* 87:4987–5016
40. Uesugi M, Kishida H (1986) Frictional resistance at yield between dry sand and mild steel. *Soils Found* 26:139–149. doi:[10.3208/sandf1972.26.4_139](https://doi.org/10.3208/sandf1972.26.4_139)
41. Uesugi M, Kishida H (1986) Influential factors of friction between steel and dry sands. *Soils Found* 26:33–46. doi:[10.3208/sandf1972.26.2_33](https://doi.org/10.3208/sandf1972.26.2_33)
42. Uesugi M, Kishida H, Tsubakihara Y (1988) Behavior of sand particles in sand-steel friction. *Soils Found* 28:107–118. doi:[10.3208/sandf1972.28.107](https://doi.org/10.3208/sandf1972.28.107)
43. Vardoulakis I (1980) Shear band inclination and shear modulus of sand in biaxial tests. *Int J Numer Anal Methods Geomech* 4:103–119
44. Vardoulakis I, Graf B (1985) Calibration of constitutive models for granular materials using data from biaxial experiments. *Géotechnique* 35:299–317
45. Vardoulakis I, Goldscheider M, Gudehus G (1978) Formation of shear bands in sand bodies as a bifurcation problem. *Int J Numer Anal Methods Geomech* 2:99–128
46. Wang J, Gutierrez M (2010) Discrete element simulations of direct shear specimen scale effects. *Géotechnique* 60:395–409
47. Wang J, Jiang M (2011) Unified soil behavior of interface shear test and direct shear test under the influence of lower moving boundaries. *Granul Matter* 13:631–641. doi:[10.1007/s10035-011-0275-2](https://doi.org/10.1007/s10035-011-0275-2)
48. Wang Y-H, Leung S-C (2008) A particulate-scale investigation of cemented sand behavior. *Can Geotech J* 45:29–44
49. Wang J, Dove JE, Gutierrez MS (2006) Determining particulate–solid interphase strength using shear-induced anisotropy. *Granul Matter* 9:231–240. doi:[10.1007/s10035-006-0031-1](https://doi.org/10.1007/s10035-006-0031-1)
50. Wang J, Dove JE, Gutierrez MS (2007) Anisotropy-based failure criterion for interphase systems. *J Geotech Geoenviron Eng* 133:599–608
51. Wang J, Dove JE, Gutierrez MS (2007) Determining particulate–solid interphase strength using shear-induced anisotropy. *Granul Matter* 9:231–240
52. Wang J, Gutierrez MS, Dove JE (2007) Numerical studies of shear banding in interface shear tests using a new strain calculation method. *Int J Numer Anal Methods Geomech* 31:1349–1366. doi:[10.1002/nag.589](https://doi.org/10.1002/nag.589)
53. Westgate ZJ, DeJong JT (2006) Evolution of sand-structure interface response during monotonic shear using particle image velocimetry. In: *Proceedings Geocongress 2006*
54. Zhang GA, Zhang J-M (2006) Monotonic and cyclic tests of interface between structure and gravelly soil. *Soils Found* 46:505–518
55. Zhang G, Zhang J (2009) State of the art: mechanical behavior of soil–structure interface. *Prog Nat Sci* 19:1187–1196. doi:[10.1016/j.pnsc.2008.09.012](https://doi.org/10.1016/j.pnsc.2008.09.012)
56. Zhao J, Guo N (2015) The interplay between anisotropy and strain localisation in granular soils: a multiscale insight. *Géotechnique* 10:184
57. Zhu H, Nguyen HN, Nicot F, Darve F (2016) On a common critical state in localized and diffuse failure modes. *J Mech Phys Solids* 95:112–131
58. Zhu H, Veylon G, Nicot F, Darve F (2016) On the mechanics of meso-scale structures in two-dimensional granular materials. *Eur J Environ Civ Eng* 20:1–24